Progress in validation of rotor aerodynamic codes using field data

Koen Boorsma[1], Gerard Schepers[1], Helge Aagard Madsen[2], Georg Pirrung[2], Niels Sørensen[2], Galih Bangga[3], Manfred Imiela[9], Christian Grinderslev[2], Alexander Meyer Forsting[2], Wen Zhong Shen[2], Alessandro Croce[4], Stefano Cacciola[4], Alois Peter Schaffarczyk[5], Brandon Lobo[5], Frederic Blondel[6], Philippe Gilbert[6], Ronan Boisard[7], Leo Höning[8], Luca Greco[10], Claudio Testa[10], Emmanuel Branlard[11], Jason Jonkman[11], and Ganesh Vijayakumar[11]

[1]TNO, Petten, The Netherlands
[2]DTU, Roskilde, Denmark
[3]IAG, Stuttgart, Germany
[4]POLIMI, Milano, Italy
[5]Kiel University of Applied Sciences, Kiel, Germany
[6]IFP Energies nouvelles, Rueil-Malmaison, France
[7]ONERA, Paris, France
[8]Fraunhofer, Bremerhaven, Germany
[9]DLR, Braunschweig, Germany
[10]CNR-INM, Rome, Italy
[11]NREL, Colorado, USA

Correspondence: K. Boorsma (koen.boorsma@tno.nl)

Abstract. Within the framework of the fourth phase of International Energy Agency (IEA) Wind Task 29, a large comparison exercise between measurements and aero-elastic simulations has been carried out featuring three simulation cases in axial, sheared and yawed inflow conditions. Results were obtained from more than 19 simulation tools originating from 12 institutes, ranging in fidelity from Blade Element Momentum (BEM) to Computational Fluid Dynamics (CFD) and compared to state of the art field measurements from the 2MW DanAero turbine. More than 15 different variable types ranging from lifting line variables to blade surface pressures, loads and velocities have been compared for the different conditions, resulting in over 250 comparison plots. The result is a unique insight into the current status and accuracy of rotor aerodynamic modeling.

For axial flow conditions, a good agreement was found between the various code types, where a dedicated grid sensitivity study was necessary for the CFD simulations. However, compared to wind tunnel experiments on rotors featuring controlled conditions, it remains a challenge to achieve good agreement of absolute levels between simulations and measurements in the field. For sheared inflow conditions, uncertainties due to rotational and unsteady effects on airfoil data result in the CFD predictions standing out above the codes that need input of sectional airfoil data. However, it was demonstrated that using CFD synthesized airfoil data is an effective means to bypass this shortcoming. For yawed flow conditions, it was observed that modeling of the skewed wake effect is still problematic for BEM codes where CFD and Free Vortex Wake codes inherently model the underlying physics correctly. The next step is a comparison in turbulent inflow conditions, which is featured in IEA Wind Task 47.

Doing this analysis in cooperation under the auspices of IEA Wind has led to many mutual benefits for the participants. The large size of the consortium brought ample manpower for the analysis where the learning process by combining several

complementary experiences and modeling techniques gave valuable insights that could not be found when the analysis is carried out individually.

1 Introduction

Wind turbine design codes are essential for the industry to assess lifetime and the energy production before the investment is made to build a turbine prototype. The aerodynamic model is then one of the most challenging components of these codes because every aerodynamic process, in its basis, is described by means of the so-called Navier Stokes equations. These equations cannot be solved in an analytical way, where also a numerical solution of the Navier Stokes equations is out of reach in design due to extreme computational demands. The difficulty of accurate aerodynamic modelling is perhaps most convincingly illustrated by the fact that solving the Navier Stokes equations (as a matter of fact 'only' proving that a smooth solution exists) is one of the seven Millenium Prize Problems as formulated by the Clay Mathematics institute in 2000 (Fefferman, 2000). As such, every aerodynamic model inherently suffers from simplifications. For wind turbine aerodynamics, an additional difficulty arises from the fact that the computational effort for design calculations is more extreme than it is for most other applications (e.g. fixed wing aerospace), see (Schepers, 2012). This necessitates the use of engineering models that are very efficient, but also very simplified aerodynamic models based on the Blade Element Momentum (BEM) method. Obviously more advanced methods like Computational Fluid Dynamic (CFD) codes are applied too, but their use is, due to the computational demands, restricted to specific studies and load cases. From a practical point of view, the simplifications in engineering methods inevitably go together with a large uncertainty band, which is even larger for modern MW-scale wind turbines. The larger uncertainties with increased rotor size are partly a result of unknown (high) Reynolds effects, where moreover the more flexible blades will lead to larger deflections and more pronounced non-linear aero-elastic behavior with unknown aerodynamic implications. Other uncertainties result from the thick(er) airfoils that are applied on large rotors, which are very difficult to model and measure accurately in an aerodynamic sense. Last but not least, the changed relation between the scales in atmospheric inflow to the scales of the turbine (blades) lead to larger uncertainties for increased rotor size.

In order to reduce the uncertainty band of aerodynamic models and to make them reliable enough for the design of cost-effective turbines, aerodynamic models need to be improved and validated with good measurements. Conventional wind turbine measurements of for example power and blade root bending moment lack sufficient detail for that purpose. More detailed sectional load information is necessary for a better validation and understanding. Historically, progress on this topic has taken advantage of international cooperation in research tasks under the auspices of IEA TCP Wind (IEA, 2021), leading to many mutual benefits for the participants. IEA Wind Task 14 and 18 contributed to this objective where field measurements from all over the world (some including sectional pressure measurements) were studied by an international consortium of wind energy researchers (Schepers et al., 1997, 2002). However, the main conclusion was that constant, uniform and controlled inflow conditions are necessary to make progress in this field, which led to several wind tunnel experiments with rotating rotors. Amongst these was Phase VI of the Unsteady Aerodynamics Experiment (UAE), testing a 2-bladed 10 m diameter wind turbine in the wind tunnel of NASA Ames Research Center, featuring a test section of 80 ft by 120 ft (Hand et al.,

2001). The measurements taken in this experiment have been subject of investigation in IEA Wind Task 20 (Schreck, 2008) and a blind comparison to simulations has been carried out (Simms et al., 2001). A follow up from these experiments was the European Union project 'MEXICO' (Model rotor EXperiments In Controlled cOnditions) in which ten institutes from six

55 countries cooperated in doing experiments on an instrumented, three-bladed wind turbine of 4.5 m diameter placed in the open section of the Large Low-speed Facility (LLF) of DNW in the Netherlands. These experiments, which also featured extensive flow field measurements using Particle Image Velocimetry (PIV), featured campaigns in 2006 and 2014 and were subject of analysis in IEA Wind Task 29 phases 1 to 3 (Schepers et al., 2012, 2014; Boorsma et al., 2018). A more detailed summary of dedicated wind tunnel experiments has recently been published online (Boorsma, 2021). Although these wind tunnels have

60 been used successfully to validate rotor aerodynamic models, translating these results to 'real life' flexible turbines in turbulent inflow conditions remains a challenge. Therefore the comparison rounds of IEA Task 29 Phase IV (Schepers et al., 2021) have focussed on newly released field measurements on a 2MW turbine from the DanAero experiment (Bak et al., 2010; Madsen et al., 2010b). The unique data from this experiment, including a description of the turbine, were made available to the participants of IEA Task 29 Phase IV so that it could form a basis for a thorough analysis. This paper presents the progress

65 of this task, where many participants from different countries simulated the same experiment. The studies may serve as a benchmark for performing code-to-code comparison involving many participants. Suggestions will be given to improve the agreement between codes.

Section 2 presents the methodology of the comparison round, including a description of the measurements and the set-up of the comparison. Sections 3 and 4 give the results of the comparison for the two cases under investigation together with a

70 discussion, which is followed by conclusions.

2   Methodology

Firstly, a description is given of the DanAero experiment. Then the setup for the comparison rounds is given, including a summary of the simulation codes.

2.1   DanAero field measurement campaign

75 Detailed aerodynamic measurements on MW-scale wind turbines are scarce and open publications about them even more so. An exception lies in the DanAero experiment (Bak et al., 2010; Madsen et al., 2010b), which was carried out in atmospheric field conditions on a NM80 2.3MW turbine in a Danish project by Danish Technical University DTU and four industrial partners (LM Glassfiber, Siemens WindPower, Vestas and Dong Energy) in two periods from 2007 until 2010 and from 2010 until 2013. At the initiation of IEA Task 29 Phase IV in 2018, the DanAero partners agreed that the measurements as well as

80 the model data for aerodynamic and aeroelastic modelling of the NM80 turbine could be shared with the partners participating in this task. The pitch controlled turbine features three LM38.2 blades resulting in a 80 m rotor diameter at 57 m hub height. The level of detail from the instrumentation lies far above the level of conventional wind turbine measurements. In addition to conventional power and loads measurement using strain gauges, surface pressures at four sections along a blade (at 13, 19, 30

and 37 m from the rotor center) were measured but also inflow velocities using pitot tubes, and a row of surface flush-mounted
microphones was installed at the outer part of the blade. Integrating the measured surface pressures around the sectional
airfoil contour resulted in the chord-normal and tangential pressure forces at these four stations. Meteorological measurements
were performed using a mast located 313 m (3.9 diameters) in southwesterly direction (237°) upwind from the turbine. The
meteorological mast included cup and sonic anemometers at 7 heights up to 93 m. An overview is given in Figure 1. More
details about instrumentation can be found in the dedicated report (Bak et al., 2013).

Figure 1. Danaero turbine and instrumentation (Bak et al., 2010)

2.2 Setup

Several cases are under investigation focusing on axial and sheared-yawed inflow, which are described in more detail below.
The comparison rounds mainly focus on the data obtained from the pressure measurements, i.e. pressure distributions and the
derived normal and tangential force at the four instrumented stations. For the CFD modelers, the blade geometry was made
available by means of a CAD file, but also a pre-processed multi-block surface and volume mesh was distributed amongst the
participants. For the lifting line codes, airfoil data was prescribed. Hereto data was obtained from dedicated wind tunnel testing
of the scanned sectional airfoil geometries of the real blade, which were 3D-corrected afterwards based on field measurements
of generator power and blade bending moments (Bak and Fuglsang, 2004). A wide variety of over 19 different codes have
been used by the participants ranging from BEM to CFD models for the rotor aerodynamics. For CFD models, both Reynolds
Averaged Navier Stokes (RANS) as well as Detached Eddy Simulation (DES) formulations have been used. But also medium

100   fidelity tools such as panel codes, actuator line (AL) and lifting line free vortex wake (LL-FVW) models are part of the comparison. An attempt to summarize the different codes has been given in Table 1. For a more detailed description of the different simulation tools used by the participants of the comparison round, the reader is referred to the code description appendix of the final report of IEA Task 29 Phase IV (Schepers et al., 2021).

Table 1. High-level summary of participant codes and settings

Legend entry	Participant	Code name	Aerodynamic model	Structural model	References
Bladed4.8_BEM	DNV-GL	Bladed4.8	BEM	multibody	(Collier, 2019)
DLR_TAU	DLR	Tau	RANS	rigid	(Schwamborn et al., 2006)
DTU_EllipSys3D	DTU	EllipSys3D	RANS	multibody (HAWC2)	(Michelsen, 1992)
DTU_AL_Shen	DTU	EllipSys3D	AL	modal (FLEX5)	(Sørensen and Shen, 2002)
DTU_AL_EllipSys	DTU	EllipSys3D	AL	rigid	(Meyer Forsting et al., 2019)
DTU_HAWC2	DTU	HAWC2	BEM	multibody	(Madsen et al., 2010a, 2020)
DTU_HAWC2NW	DTU	HAWC2	BEM plus nearwake	multibody	(Pirrung et al., 2016, 2017)
FW_IWES_Emden	Forwind	OpenFOAM	RANS, DES	rigid	
IFPEN_BEM	IFPEN	DeepLines Wind^{TM}	BEM (*AeroDeeP*)	multibody	(Le Cunff et al., 2013; Perdrizet et al., 2013)
IFPEN_VL	IFPEN	DeepLines Wind^{TM}	LL-FVW (*CASTOR*)	multibody	(Bozonnet et al., 2017; Blondel et al., 2018)
INM_FUNAERO	CNR-INM	FUNAERO	Panel code	rigid	(Greco and Testa, 2021)
NREL_ED	NREL	OpenFAST	BEM (AeroDyn)	modal (ElastoDyn)	(Moriarty and Hansen, 2005)
NREL_VC	NREL	OpenFAST	LL-FVW (OLAF)	modal (ElastoDyn)	(Shaler et al., 2020)
NREL_CFD	NREL	Nalu-Wind	RANS	rigid	(Sprague et al., 2019)
ONERA_PUMA	ONERA	PUMA	LL-FVW	rigid	(Mudry, 1982)
ONERA_ElsA	ONERA	ElsA	RANS	rigid	(Cambier L., 2008)
PhatAero_BEM	TNO	AeroModule	BEM	multibody (Phatas)	(Boorsma et al., 2011)
PhatAero_AWSM	TNO	AeroModule	LL-FVW (AWSM)	multibody (Phatas)	(van Garrel, 2003)
PoliMi_Cp-Lambda	PoliMi	Cp-Lambda	BEM	multibody	(Bauchau et al., 2001)
UAS_Kiel_Tau	UAS Kiel	Tau	RANS	rigid	(Schwamborn et al., 2006)
USTUTT_FLOWer	USTUTT IAG	FLOWer	RANS, DES	rigid	(Kroll et al., 2000)

The distribution of chord-normal and tangential forces along the blades is supplied by all participants, together with rotor
105   axial force and torque. For the CFD and panel codes, also pressure distributions are compared to the measurements. The lifting line codes that use airfoil data also supplied the distribution of so-called 'lifting line variables' (angle of attack, effective wind speed and induced velocities), which are compared between the simulations only. To improve the comparison of the results, also

non-dimensionalized values of normal and tangential force are compared. These are non-dimensionalized using undisturbed local dynamic pressure (determined from wind and local rotational speed) to allow for a solid comparison of airfoil coefficients
110 between experiment and simulations along the span without the complications of uncertainty in rotor induced velocities. Hence the definition for the non-dimensionalized normal force, which is equivalent for the tangential force, can be given as

$$\text{Fnc\_qc} = \frac{\text{Fn}}{0.5\rho(U_\infty{}^2 + (\omega r)^2)c}, \quad \text{with} \tag{1}$$

Fnc_qc	[-]	Non-dimensionalized chordnormal force
Fn	[N/m]	Chordnormal force
ω	[rad/s]	Rotor speed
ρ	[kg/m^3]	Air density
U_∞	[m/s]	Wind speed
r	[m]	Local radius
c	[m]	Local chord.

115 The supplied axial force and torque have been post-processed to thrust and power coefficients Cd_{ax} and Cp using

$$\text{Cd}_{ax} = \frac{\text{Fax}}{0.5\rho U_\infty{}^2 \pi R^2}, \quad \text{and} \quad \text{Cp} = \frac{\text{Torque}\ \ \omega}{0.5\rho U_\infty{}^3 \pi R^2}, \quad \text{with} \tag{2}$$

Cd_{ax}	[-]	Axial force coefficient
Cp	[-]	Power coefficient
Fax	[N]	Rotor axial force
Torque	[Nm]	Rotor torque
R	[m]	Rotor radius.

For the axial flow case, the aerodynamic flatwise moment is deduced using a script that linearly integrates the simulated
120 force distribution along the blade span. For the yawed and sheared case, the flatwise moment was directly supplied by the participants. The displayed experimental values have been obtained from the post-processed strain gauge measurements by removing gravity and inertial contributions.

3 Case IV.1: Axial uniform inflow

The first case, IV.1, is summarized in Table 2, based on a measurement data point in summer 2009 with relatively steady
125 and uniform inflow and constant operational conditions. It can be observed that the turbine is highly loaded with an average value of 0.38 for the axial induction factor, which is generally considered to be the turbulent wake state. Unfortunately no measurement data was available with the turbine operating at a lower induction factor. For this case, the tilt angle (5°) and tower shadow effects are neglected by the modelers, but blade pre-bend is included. The case is subdivided into Case IV.1.1 where the turbine (i.e. tower, blades etc.) should be modeled rigid, and Case IV.1.2 where flexibility is included. It is noted

6

130 that although a comparison is made with the measurements (for which the blades are obviously flexible), the CFD simulations
were mostly performed for a rigid blade.

**Table 2.** DanAero comparison cases (axial flow)

Case nr	Model	Wind speed U_∞ [m/s]	Pitch angle [°]	Rot. speed ω [rpm]	Tip speed ratio λ [-]	Angle of attack $\alpha^\dagger$ @80%R [°]	Axial induction factor $a^\dagger$ @80%R [-]
IV.1.1	Rigid	6.1	0.15	12.3	8.4	4.0	0.38
IV.1.2	Flexible	6.1	0.15	12.3	8.4	4.0	0.38

† estimate

3.1 Lifting line codes

Selected *lifting line variables* comparison plots for Case IV.1.2 are given in Figure 2. These variables are calculated for
all codes that need the input of sectional airfoil data. The effective velocity Ueff (a composite of wind, motion and rotor
135 induced velocities) is in good agreement between the codes, indicating that the inputted operational conditions are consistent
between the codes. Small differences can be observed in the inboard region, where induction starts to play a role over the
elsewhere dominant rotational velocity. The angle of attack AOA shows larger variations, caused by the differences in axial
and tangential induced velocities Ui and Vi, as shown in Figures 2c and 2d. A closer look at the axial induced velocity Ui
shows that, especially apparent for the participants that delivered both BEM and free vortex wake results, the free vortex wake
140 codes (usually depicted with a dashed line) feature a roughly 10% lower induced velocity. A similar observation was made in
the final report of Mexnext-III (Boorsma et al., 2018) for the New Mexico case in the turbulent wake state, which featured a
high axial induction factor similar to the case under investigation here.

The resulting *loads* in terms of non-dimensionalized sectional normal and tangential force Fn and Ft are given in Figure 3.
Consistent with the induced velocities and angles of attack, the agreement in Fn is fair between the computational results, with a
145 spread around 5%. A closer look at the levels in Figure 3a again shows a difference between vortex wake codes and BEM codes,
where the latter generally feature a lower loading than vortex code results. This is also reflected in the integral performance
from Figures 3c and 3d (blade root flatwise moment, axial force and power). Acknowledging the earlier observed variations
in axial induced velocities, this discrepancy seems to be in contradiction with momentum theory, where a higher loading is
accompanied with more induction. However this could also be attributed to uncertainties in the engineering extensions used
150 for the turbulent wake state in which the turbine is operating for this case. Grouping the results by code type, as will be shown
in section 3.3, allows to better observe the loading differences.
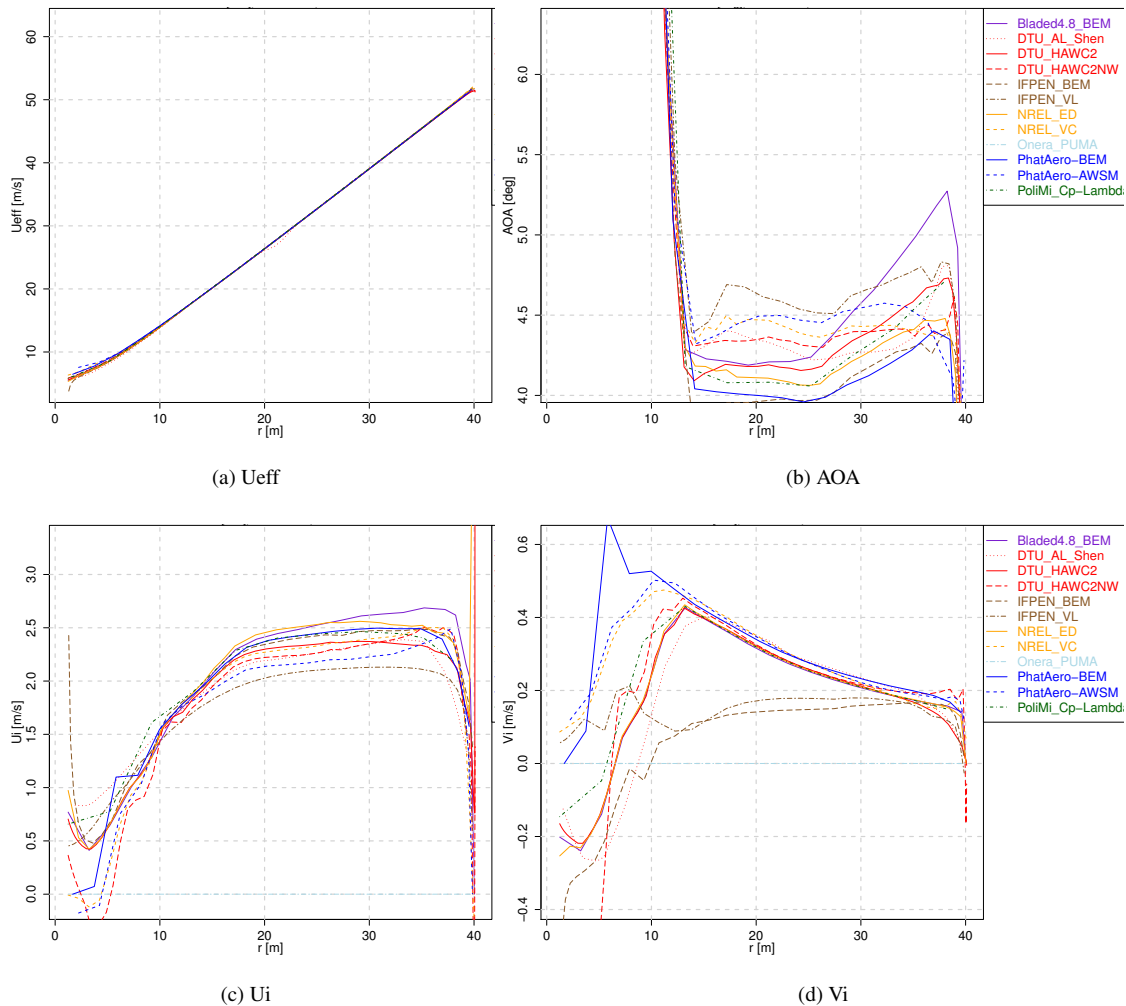
Figure 2. Lifting line variables for Case IV.1.2

The comparison with measured values (obtained from the integration of the measured pressure distributions) shows the normal force to be consistently overpredicted by approximately 10% for all radial positions. It could then be expected that this overprediction is reflected in the measured flatwise moments from Figure 3c as well. However, the observed differences for this moment are around $\pm\ 2\%$, where it should be noted that the measured flatwise moments are obtained from the strain gauge rather than the pressure measurements. Detailed investigations of possible causes for the low experimental normal force were carried out during IEA Task 29 Phase IV , unfortunately without success. Contrary to the normal force, the tangential force (Figure 3b) reveals an under, instead of over prediction. Here it must be noted that the measured values only contain the contribution of pressure, whereas the simulations are based on airfoil coefficients, which also contain the friction forces. For the tangential direction, this contribution is significant (as will be shown in section 3.2) and taking this into account will result

in a better agreement between measurements and simulations. In addition to that, it is known that obtaining tangential force from integration of a finite number of pressures is very sensitive to the distribution of the taps, especially around leading and trailing edge. In summary, tangential forces obtained from pressure distributions should be interpreted with care.

Figures 3e and 3f then display the predicted *deformations* between the aero-elastic codes. Here it is shown that besides some outliers, most codes agree within 1% for the flapwise deformation (dx), whereas there is a bit more scatter in the edgewise deformation (dy). However, in absolute sense, we are comparing differences of less than a centimeter. As some of the participants did not provide results for the flexible case (IV.1.2), several colors are visible on the zero line. Although not depicted here, the differences due to the flexibility between Case IV.1.1 and IV.1.2 are mostly noticeable in the outboard region of the blades. Because of the flapwise prebend, which is 'flattened' for the flexible case, the wind faces the blades more head-on and the radius is slightly increased, resulting in slightly larger loads (and larger effective velocity, induced velocities and angle of attack) toward the tip.

(a) Fnc_qc

(b) Ftc_qc

(c) Flapwise moment Mflat

(d) Performance

(e) Flapwise deformation dx

(f) Edgewise deformation dy
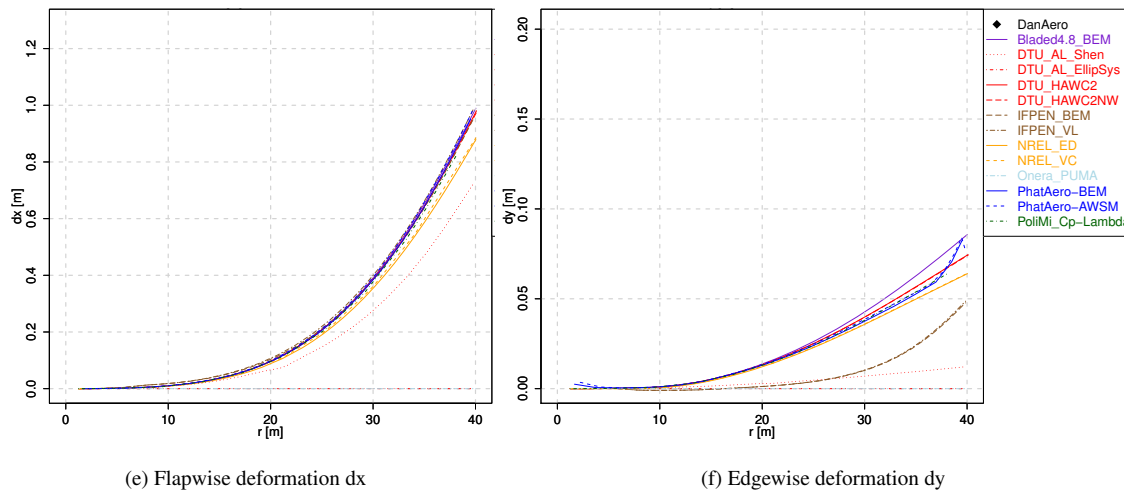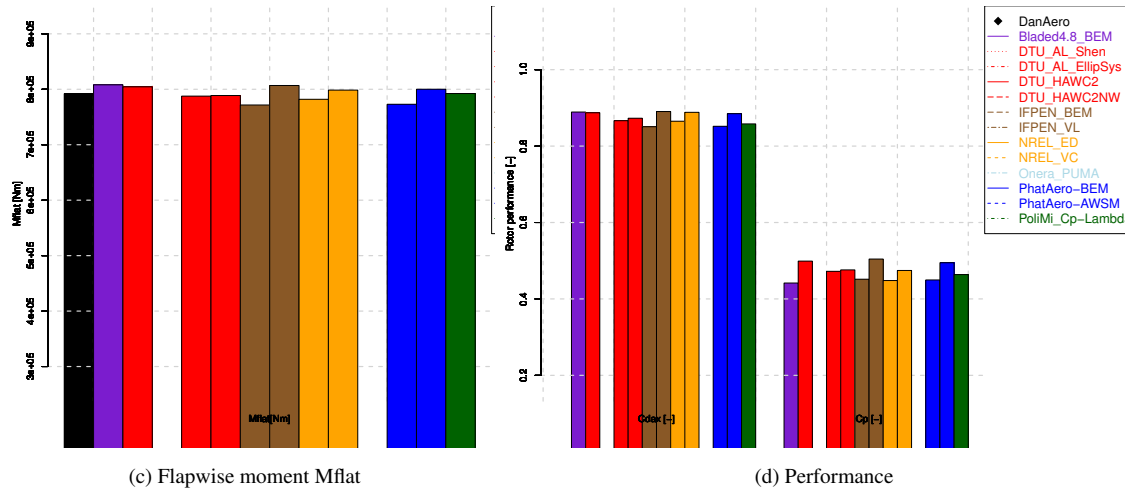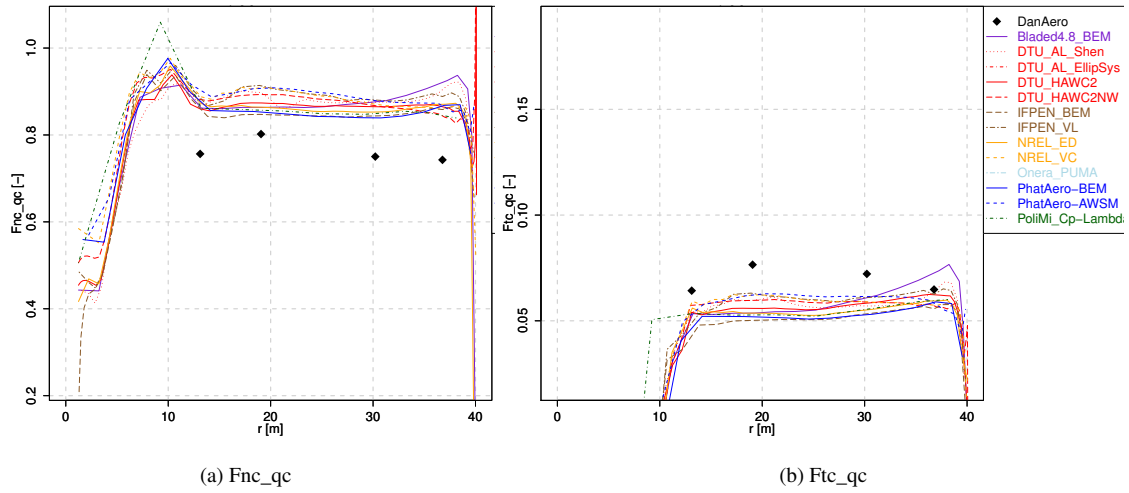
Figure 3. Loads, performance and deformations for Case IV.1.2. Note that for the bar plots the order of the bars agrees with the order of the legend entries.

3.2 CFD and panel codes

Starting with a comparison of the ***sectional geometries*** used by the codes, Figures 4a and 4b show the shapes of the most in- and outboard section. Theoretically these shapes should be identical, but some offsets appear and in some cases even local twist differences are apparent. The question remains whether these deviations are due to different ways of post-processing (e.g. a different orientation or location of the section) or if the geometries are not identical. As the blade geometry was prescribed by an IGES file, the latter should not be the case. It is acknowledged that retrieving a sectional blade slice in a 3D pre-bended rotor geometry can result in differences due to small inconsistencies like definition of radial coordinate, angular orientation of the sectional plane and direction of the chord line. What adds to that is the fact that different software packages are being used together with the corresponding 'human factor'. Hence it can be considered evident that differences appear, which is representative for what happens in real life CFD applications.

The ***pressure distribution*** comparison plots from Figure 4 show the models tend to agree well for all radial positions, although the inviscid panel code is unable to predict separated flow in the most inboard station in Figure 4c. But at this station, the CFD codes also struggle to match the measured pressure distribution on the suction side just before the trailing edge. For the other three radial positions, the suction levels are 5% to 10% higher in comparison to the experiment. Acknowledging the fact that most CFD codes model the boundary layer fully turbulent (whereas the experiment features free transition), this is contrary to expectation. At r=30.20 m (Figure 4e), the linear shape of the measured pressure distribution on the pressure side just before the chordwise position of maximum thickness differs from the rounded shape, as predicted by all simulations. A separate sectional study was performed by DTU to compare the performance between design and measured geometries, of which the first was used for this comparison round. This however revealed very small differences in comparison to the differences shown here. Besides these small deviations, one can conclude that generally speaking the pressure distributions are in good agreement between simulations and between simulations and experiment.
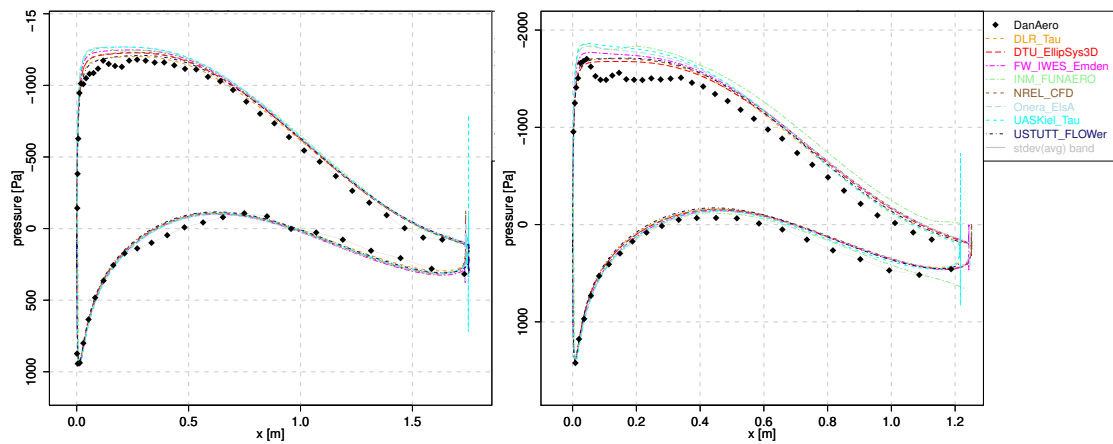
11
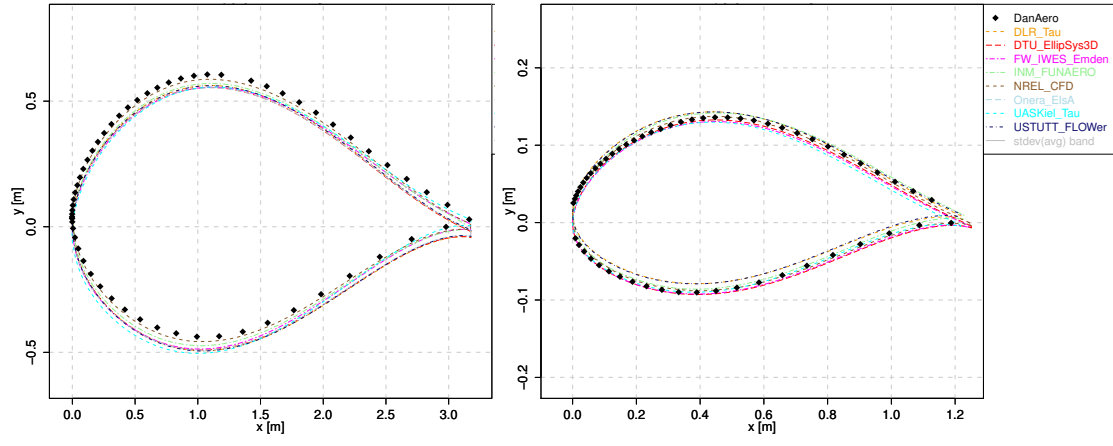
(a) Sectional geometry at r=13.12 m

(b) Sectional geometry at r=36.78 m
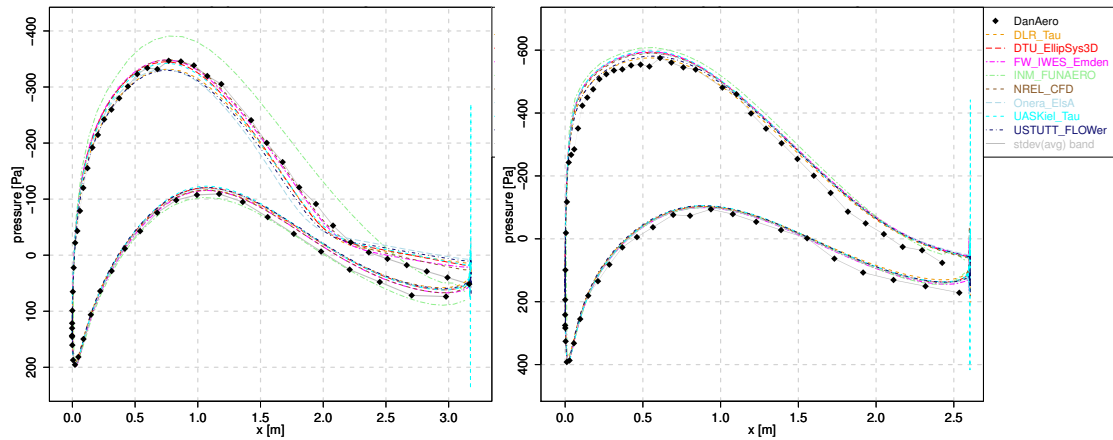
(c) Pressure at r=13.12 m

(d) Pressure at r=19.06 m

(e) Pressure at r=30.20 m

(f) Pressure at r=36.78 m

Figure 4. Sectional geometry and pressure distributions (Case 1.1)

To further dive into the observed discrepancies between the CFD codes, a ***sensitivity study*** was carried out by DLR, DTU, UAS Kiel and IAG University of Stuttgart. Hereto their CFD results were post-processed using a common tool at IAG to

195 improve the consistency between the CFD simulations. Additional simulations were run using a finer mesh resolution to asses the impact of the grid resolution. The properties of the coarse and fine mesh are summarized in Table 3. Here it is noted that DTU used a fine mesh with full rotor topology, while the others used a periodic boundary condition. Although for the periodic

Table 3. Coarse and fine mesh properties

Name	Topology	Total nr of cells [M]	First cell normal size [m]	Chordwise nr of cells [-]	Spanwise nr of cells [-]	Domain size [D]	Participants
Coarse	full rotor (360°)	14	1.0×10^{-6}	256	128	10	DLR, DTU, IAG, UAS Kiel
Fine	full rotor (360°)	113	0.5×10^{-6}	512	256	10	DTU
Fine	blade periodic (120°)	26	2.0×10^{-6}	256	200	10	DLR, IAG

fine mesh. the chordwise resolution is the same as the coarse mesh and the first cell normal size is even larger, the total number of cells for a full rotor equivalent of this mesh would roughly differ by a factor of 6 ($26\times3/14$). Hence, the majority of the extra

200 cells for this fine mesh are placed in the wake and the background mesh.

In addition to the grid sensitivity study, the results of the coarse and fine mesh were post-processed to observe the contribution of friction to the integrated forces. The following results can then be visualized:

cf   coarse mesh, friction and pressure forces included

cp   coarse mesh, pressure forces only

ff   fine mesh, friction and pressure forces included

fp   fine mesh, pressure forces only.

The resulting comparison plots are shown in Figure 5. For the DTU result in Figures 5a and 5b, it becomes clear that the mesh

205 refinement hardly has an influence on the results and the coarse mesh suffices. For the IAG University of Stuttgart results in Figures 5c and 5d, this conclusion does not hold, and level differences up to 10% can be observed. The same holds for the DLR results (which are not shown here for the sake of briefness). While the coarse mesh is already providing grid independent results for the incompressible DTU EllipSys3D solver, the compressible solvers require further refinement. Although the underlying pressure distributions are not shown here, the compressible codes reveal a different pressure level on the suction side between

210 the coarse and fine mesh results, which causes the differences in the shown sectional loads as obtained from the integrated pressure distributions. A similar finding was previously reported in the EU AVATAR project Hansen et al. (2016). Figures 5e

13

and 5f demonstrate that refining the mesh improves the consistency between the codes significantly. Apart from the blade root region inboard of 10 m span, the results are close to identical.

As expected, the effect of friction is hardly present in the normal force, which can be deduced from Figures 5a and 5c. For the tangential force this is different, especially for the three most outboard stations that feature moderate angles of attack with attached flow. The friction reduces the tangential force by approximately 15%, consistent between the two code results displayed here.

(a) Fnc, DTU

(b) Ftc, DTU

(c) Fnc, IAG

(d) Ftc, IAG

(e) Fnc, fp

(f) Ftc, fp
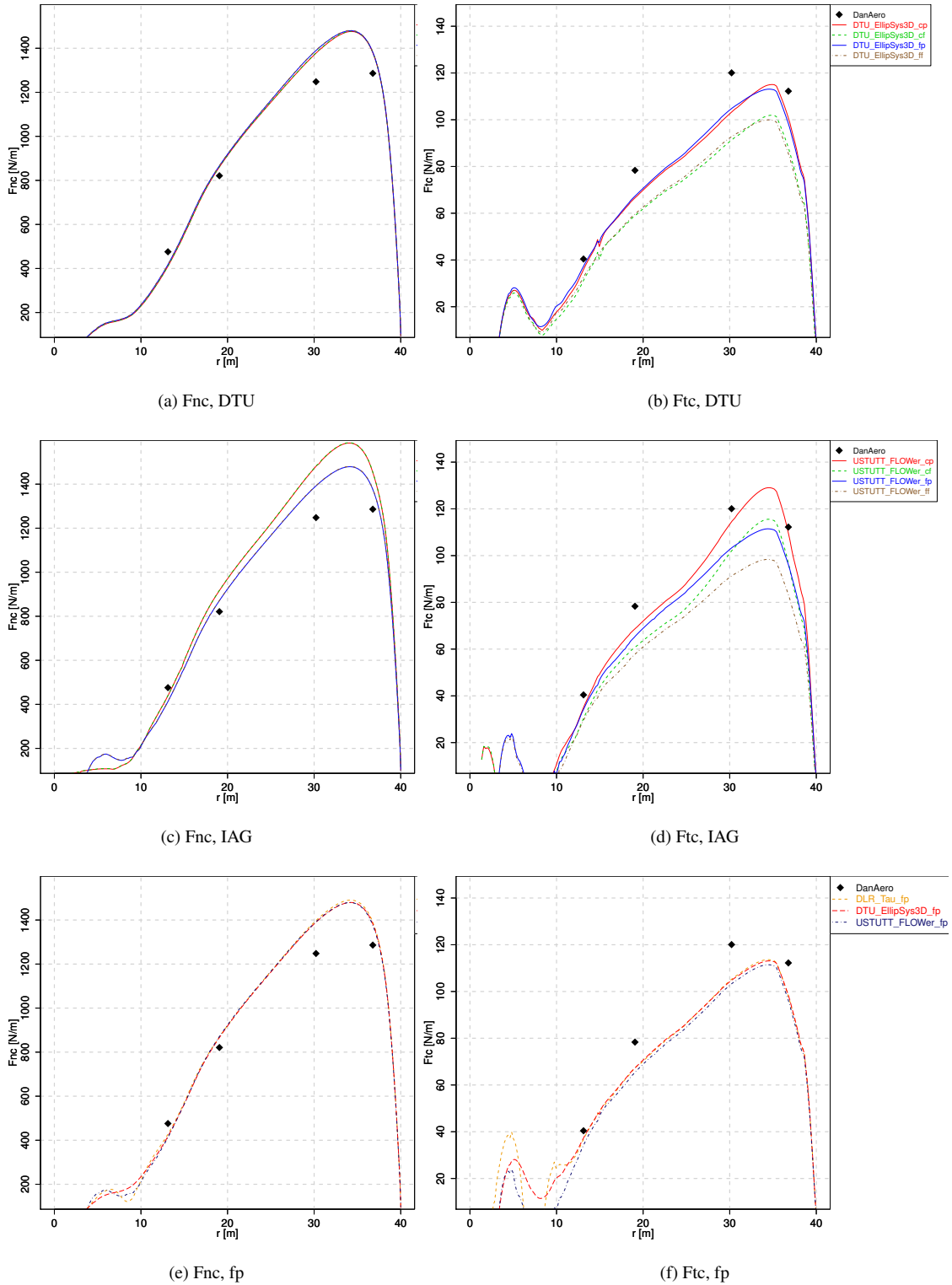
Figure 5. Effect of CFD sensitivity studies on predicted loads for Case IV.1.1

3.3 Model types comparison

In addition to displaying the loading results from the various codes, the supplied data also give the opportunity to calculate an
average result for each code type. Here the following code types are distinguished:

- BEM

  Blade Element Momentum methods using the prescribed airfoil data set.

- FVW

  Lifting line free vortex wake methods, also using the prescribed airfoil data.

- CFD

  Computational fluid dynamics codes, which model the rotor blade geometry and the 3D space around it. In most cases, the blade boundary layer is modeled as fully turbulent to promote consistency between the results.

In addition to the code types listed above, there are also a panel code and actuator line codes that joined the comparison round, but they were excluded from the averaging as the number of codes for these types are deemed too few (<3) to obtain valuable statistics.

To obtain the loading averages, first the normal and tangential force are determined at the same spanwise four positions as the instrumented sections using linear interpolation from the supplied radial distributions. A simple average $\overline{x}$ and standard error x_{err} between the supplied results of a code type are determined using

$$\overline{x} = \frac{1}{n}\sum_{i=1}^{n}(x_i) \qquad \text{and} \quad x_{err} = \sqrt{\sum_{i=1}^{n}\frac{(x_i - \overline{x})^2}{n(n-1)}}, \quad \text{with} \tag{3}$$

x_i sample value

$\overline{x}$ average

x_{err} standard error

n number of samples.

To give an indication of the variability between the results, a partly transparent band is plotted around the average of each code type illustrating the standard error x_{err} between the supplied results of a code type. The same procedure is applied to the flatwise moments, axial force and torque (average levels only). This process is only performed for the rigid results because the largest number of CFD results is provided for this configuration.

The results are illustrated in Figure 6. One can conclude that the level of the normal force generally agrees within 5% between the different code types. Acknowledging the fact that we are operating in the turbulent wake state and BEM codes need an empirical relation to replace momentum theory, this difference between the code types is considered small. The same holds for the variability between the BEM codes, as different empirical relations exist that describe the turbulent wake state. Besides this observation, the tip region shows more of a fall-off for CFD and the root region features a sudden drop in level for

16

the CFD results. Here it is noted that most BEM codes feature a Prandtl tip correction to correct for the non-uniformity between the blades (which is intrinsic to the FVW codes). It can be hypothesized that the larger load fall-off in the tip region for CFD is related to the decambering effect on the tip sections of a finite blade, which is not properly accounted for by lifting line codes. The higher loading for free vortex wake models as discussed in section 3.1 is also apparent from the plots. For the tangential force, the differences between the code types are larger, but in absolute sense these are rather small. The reason for the good trend overlay between CFD and FVW opposed to BEM is not fully understood and could as well be attributed to coincidence. The bands showing the variability between results from each code type are similar between the different types and amount to $\pm 1\%$ for the normal force and $\pm 5\%$ for the tangential force. In the previous phases of IEA Task 29, the 'human factor' would result in a larger spread between CFD results. The dedicated efforts to minimize this spread as described in section 3.2 seem to have paid off together with the fact that multiple iterations were performed to eliminate errors.

Comparing against the measurements, the normal force is overpredicted by approximately 10% for almost all sections, while the flatwise moment agrees within $\pm 2\%$ as was observed in the dedicated section discussing lifting line code and CFD results. For the discussion on the tangential force discrepancy, the reader is referred to the lifting line code discussion in section 3.1.

(a) Fnc_qc

(b) Ftc_qc

(c) Mflat

(d) Performance
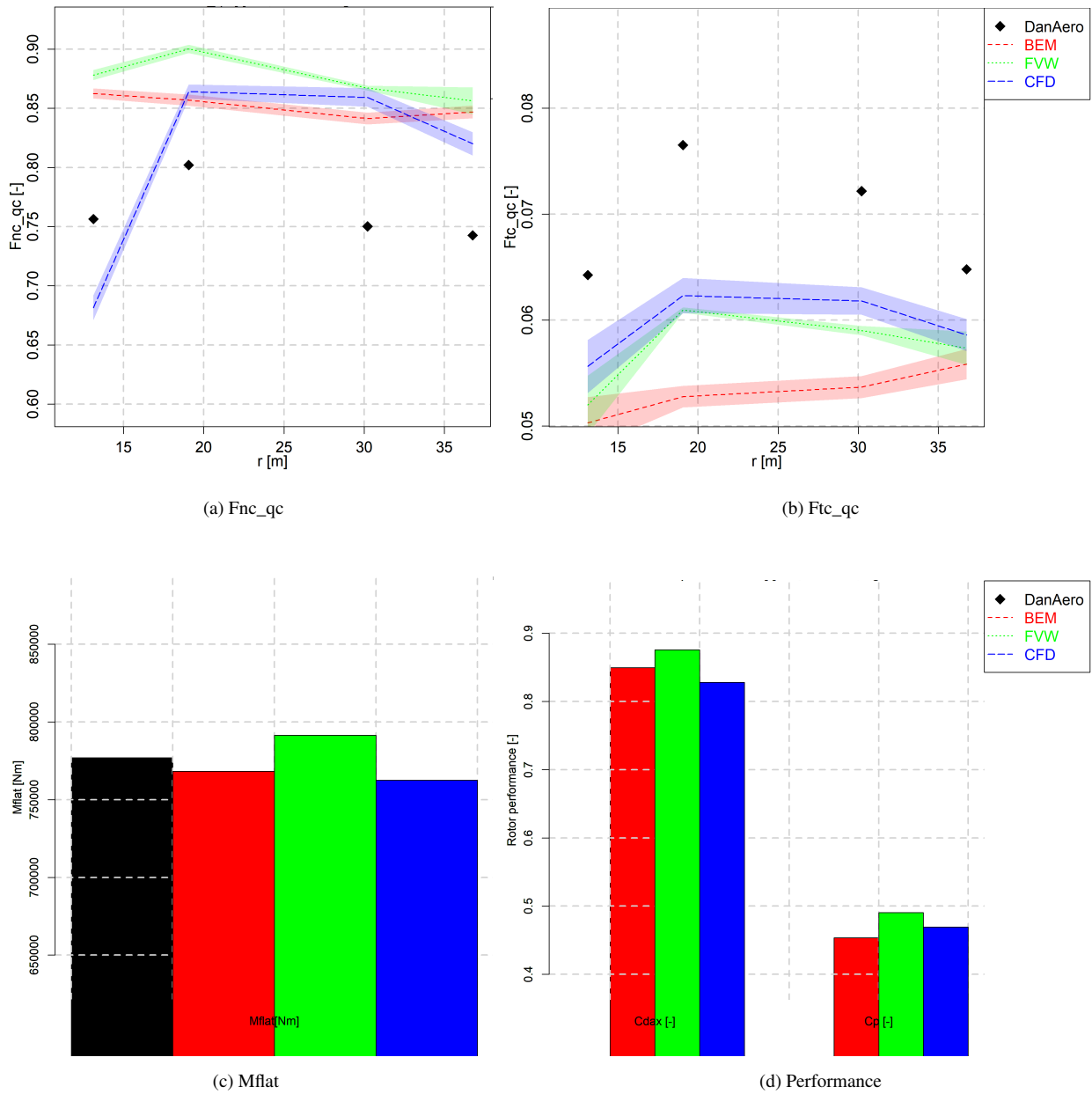
Figure 6. Loads comparison by model types for Case IV.1.1

4 Case IV.2: Sheared and yawed inflow

260 Two cases are defined featuring a significant vertical wind shear and yaw misalignment (also including vertical shear) as summarized in Table 4, carefully selected from the available measured time series. Again it can be observed that the turbine is

18

highly loaded and operating in the turbulent wake state for both cases. For these cases, flexibility, tilt angle and tower shadow effects are included. Although the flexibility was accounted for in the BEM and FVW simulations, it was anticipated that for many CFD contributions this was not manageable (a rigid and tilted rotor without the tower effect will suffice for CFD).

265 However, the main priority here is comparison to the measurements, and, fortunately an investigation using a stiff and flexible aero-elastic model of the turbine in simulations indicated that the flexibility had a very small impact on the aerodynamic blade force variation. As we are studying the load variation due to shear and yaw, the results are presented as a function of rotor azimuth angle. To better compare the loads trends as a function of the azimuth angle, the mean over the rotor revolution has been subtracted from these results now showing a 'delta'. For the measurements, because results over multiple revolutions are

270 available, the standard deviation between these measured values gives an indication of the repeatability. The standard deviation is indicated in the graphs by a grey band around the mean value.

Table 4. DanAero comparison cases (shear and yawed flow)

Case nr	Shear exponent	Wind speed U_∞ [m/s]	Yaw angle [°]	Pitch angle [°]	Rot. speed [rpm]	Tip speed ratio λ [-]	Angle of attack $\alpha^\dagger$@80%R [°]	Axial induction factor $a^\dagger$@80%R [-]
IV.2.1	0.249	9.792	-6.02	-4.75	16.2	6.9	10.0	0.41
IV.2.2	0.262	8.429	-38.34	-4.75	16.2	8.1	7.0	0.42

† Estimate of azimuth averaged value

4.1 Pressure distributions

Pressure distributions at 0° azimuth are given for all four radial stations in Figures 7 and 8 for Case IV.2.1 and IV.2.2 re-spectively. Also note that animations featuring four different azimuth angles (0°, 90°, 180° and 270°) are available from the

275 supplement. Generally speaking the trend with azimuth is well captured, but the separated flow conditions for Case IV.2.1 (especially inboard) are a challenge for the panel code and some of the CFD codes. For both cases, the measured pressure distributions at 92%R (Figures 7d and 8d) feature a dip at the suction side around 20% chord, which seem rather fierce to be introduced by transition. It is noted that for these dynamic cases involving shear, most of the CFD modelers employed a different meshing strategy in comparison to the uni-axial case. More details can be found in the detailed code descriptions from

280 the final report (Schepers et al., 2021).

(a) r/R=33%

(b) r/R=48%

(c) r/R=76%

(d) r/R=92%
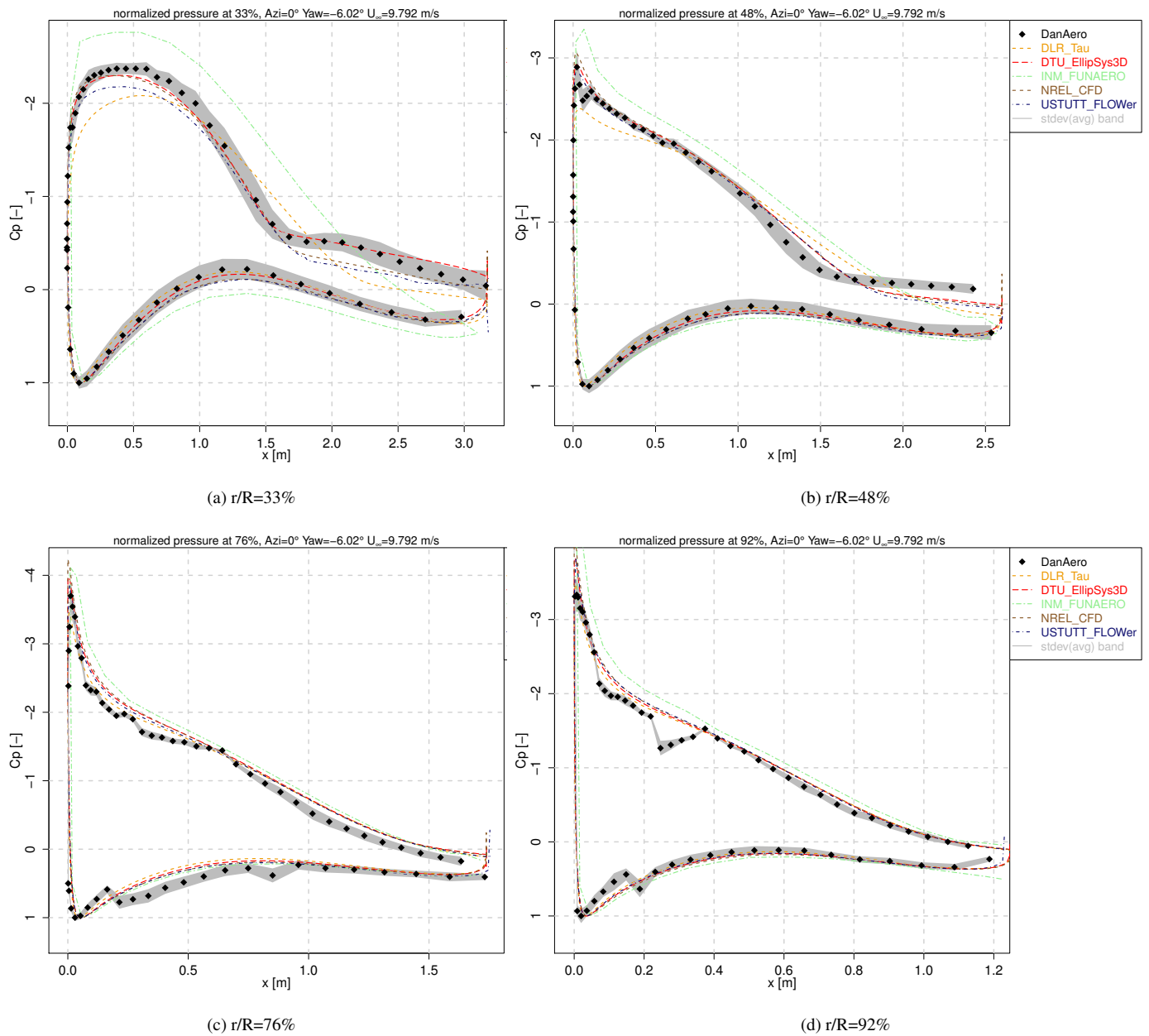
Figure 7. Pressure distribution comparison at zero degree azimuth angle, Case IV.2.1. Animations of variation with azimuth angle are available from the supplement.

(a) r/R=33%

(b) r/R=48%

(c) r/R=76%

(d) r/R=92%
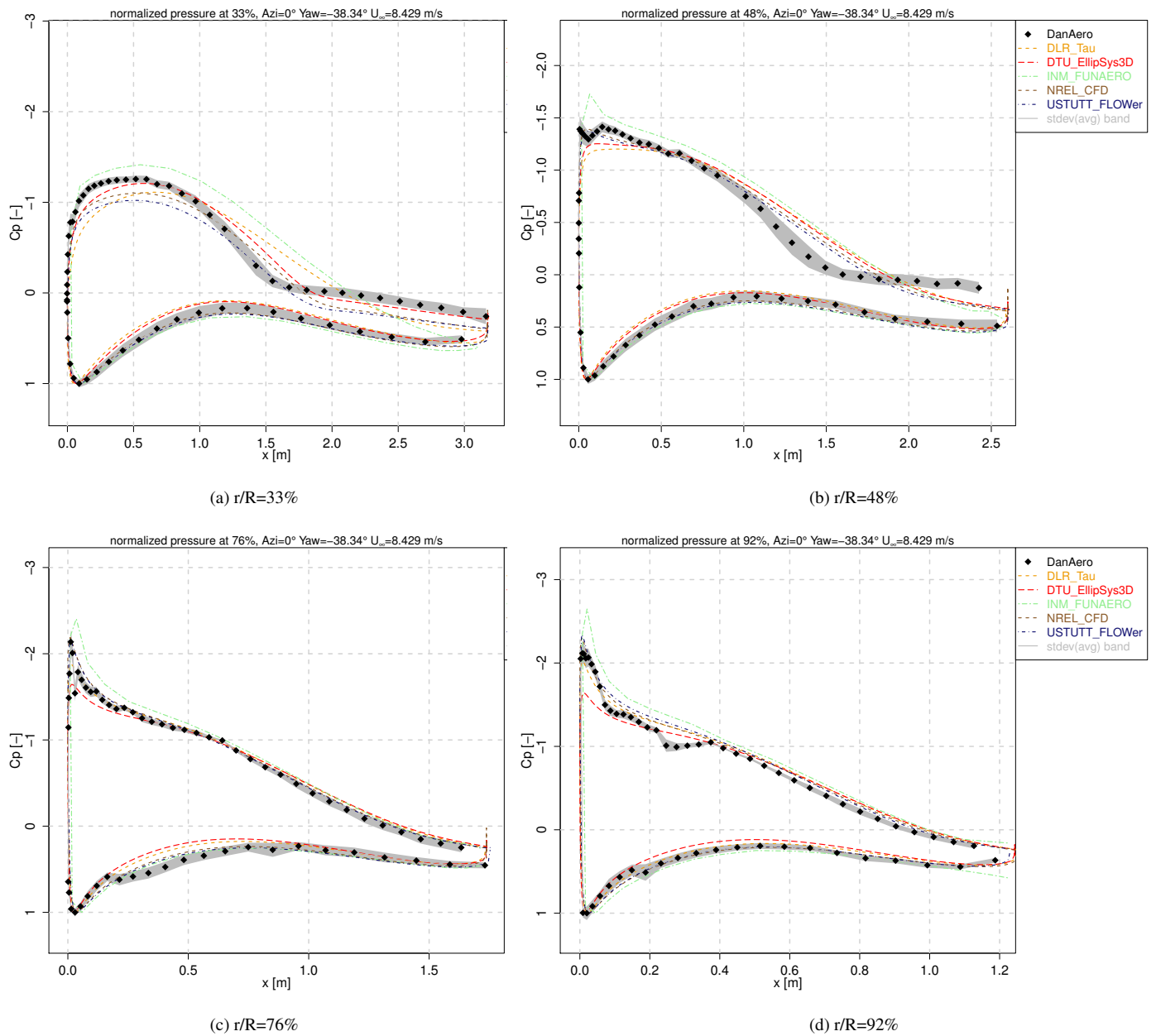
Figure 8. Pressure distribution comparison at zero degree azimuth angle, Case IV.2.2. Animations of variation with azimuth angle are available from the supplement.
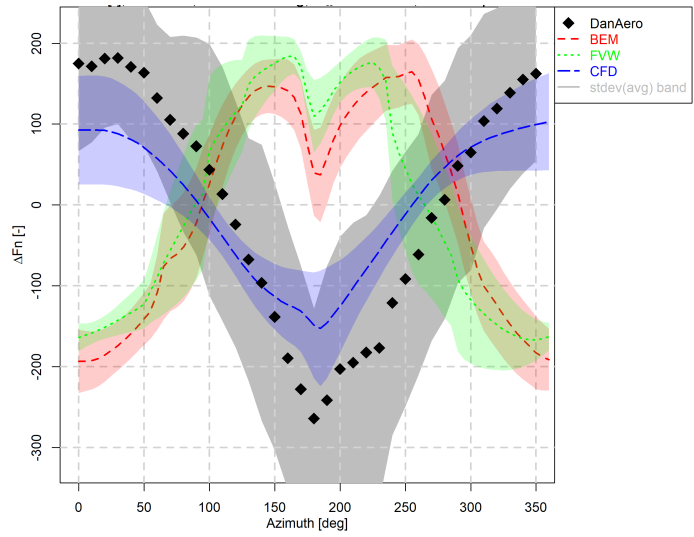
4.2 Model types

Similar to the axial flow analysis described in section 3.3, results between code types have been averaged to give a better overview of the differences between them. To obtain the loading averages and standard error, the same data reduction procedure is adopted as for axial flow. Because we are interested in the load variation as a function of azimuth, all supplied code results are linearly mapped onto an azimuth angle distribution with a 5° step, prior to calculating the average and standard error for each code type.

The results in terms of normal force variation are illustrated in Figures 9 and 10. Although the average level of the result is removed since we are focusing on the azimuthal variation, these were mostly in line with the differences observed in the Case IV.1 in axial inflow. The trends for the sheared case in Figure 9 clearly illustrate the benefit of CFD simulations over the lifting line codes. The variability within each code type (as illustrated by the colored band around the mean results) is of the same order for all code types for this case, although there seems to be a significant variability in the amplitude of the dip around 180° azimuth as predicted by CFD codes.

The yawed case shows different trends, as it is dominated by induction rather than airfoil aerodynamics. This is illustrated by the normal force in Figure 10, with a maximum near 270° azimuth for the outer part of the blade and near 90° azimuth for the inner part. This is explained by induction effects from the skewed wake, see (Schepers, 2012): At the inner part of the blade the azimuthal load variation at yawed conditions is mainly determined by the induction from the skewed root vortex, whereas the load variation at the outer part of the blade is mainly determined by the induction from the skewed tip vortex, which gives a 180° different phase shift to the induction (and resulting load) variation. This skewed wake effect is inherently modelled by CFD and vortex methods by which they almost completely fall within the experimental uncertainty band, especially for the outboard sections. BEM codes rely on uncertain engineering methods to model these skewed wake effects by which the variability between BEM codes is more than two times larger than vortex and CFD codes.
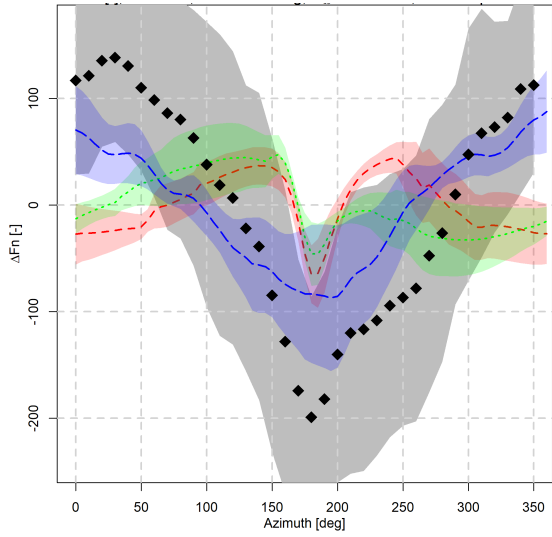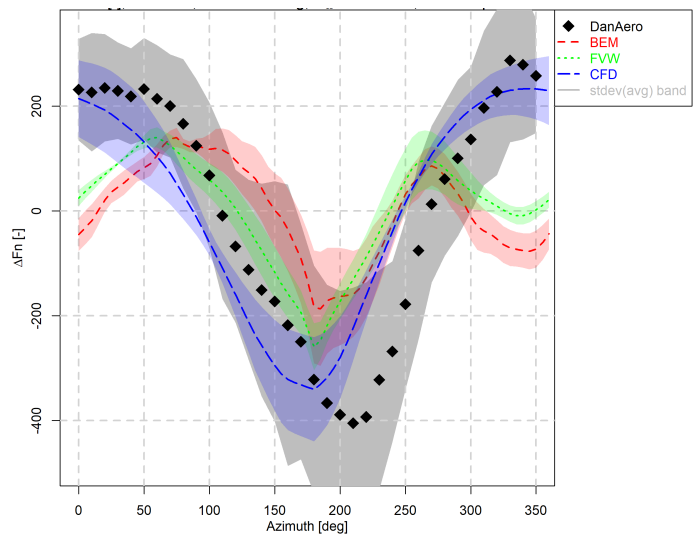
(a) Fn, r/R=33%

(b) Fn, r/R=48%
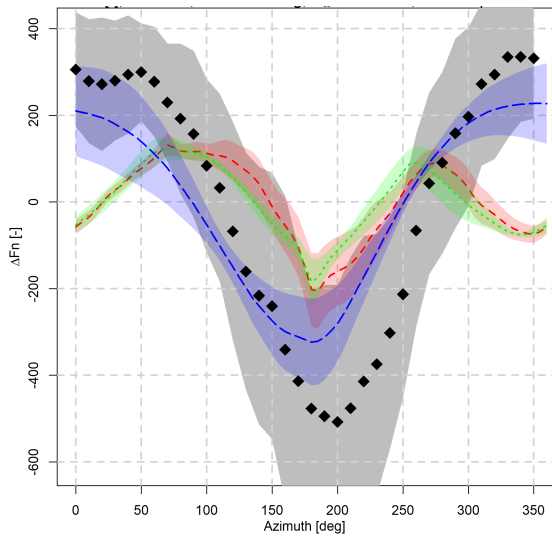
(c) Fn, r/R=76%
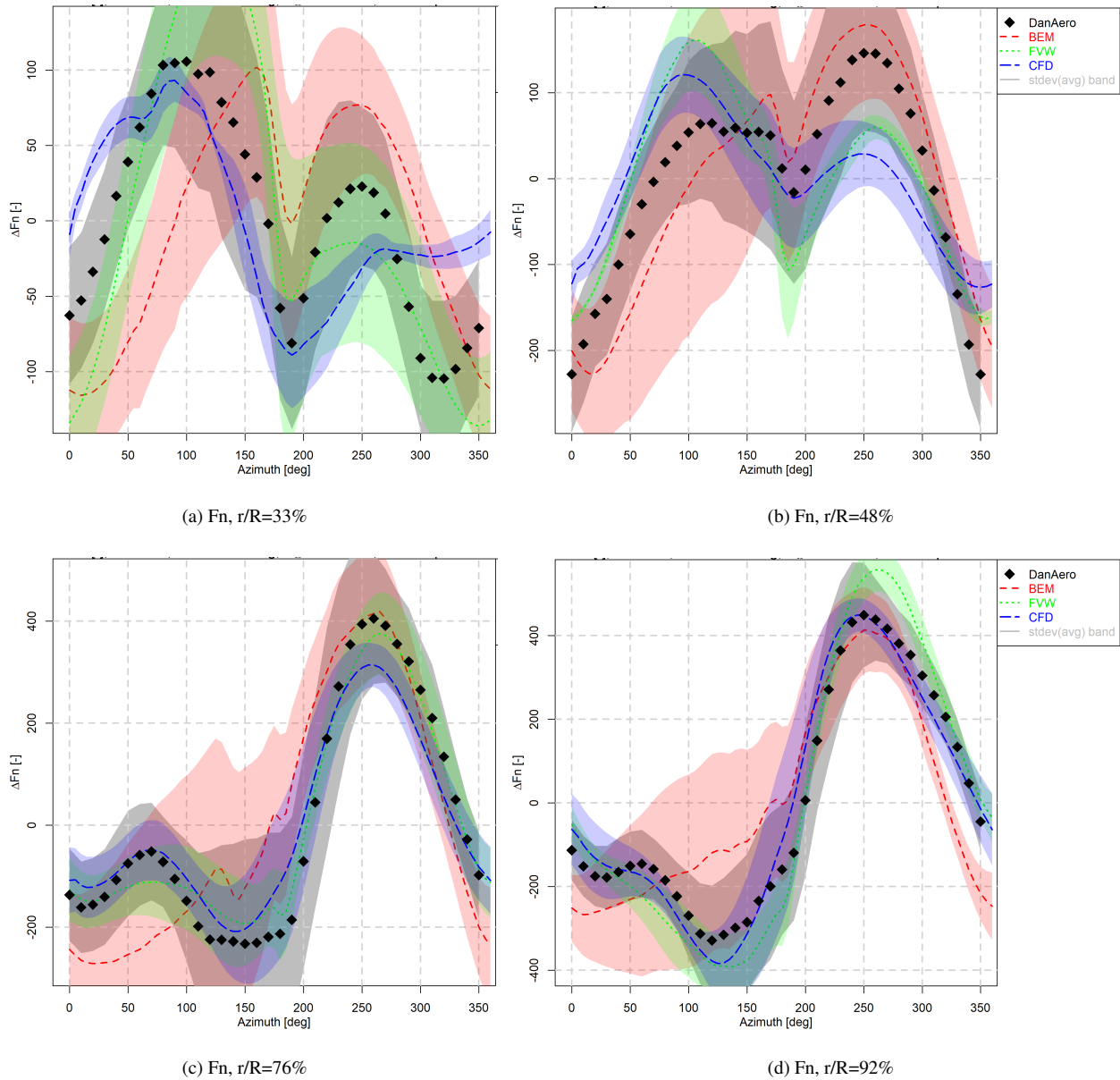
(d) Fn, r/R=92%

Figure 9. Normal force Fn variation by model types, Case IV.2.1

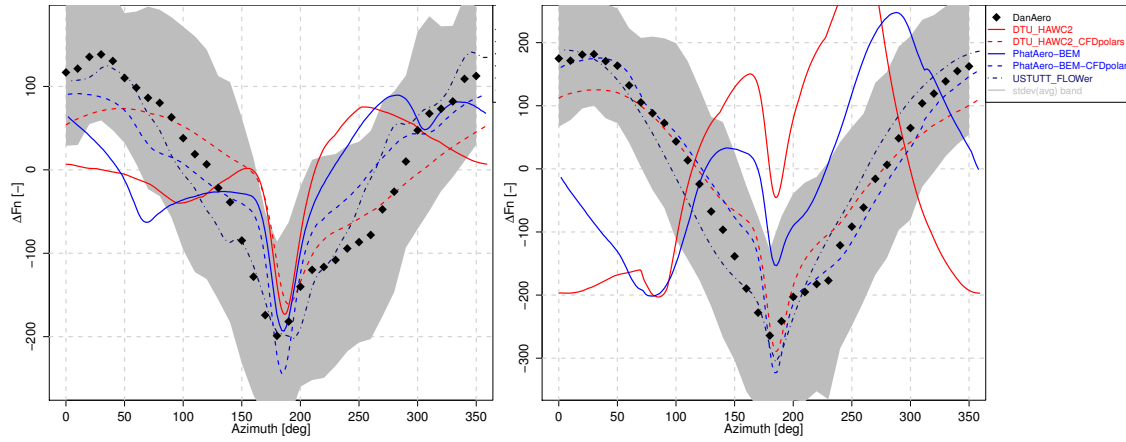(a) Fn, r/R=33% (b) Fn, r/R=48% (c) Fn, r/R=76% (d) Fn, r/R=92%

Figure 10. Normal force Fn variation by model types, Case IV.2.2

4.3 CFD synthesized airfoil data

The poor agreement of lifting line codes with measurements for the shear case together with the encouraging CFD results instigated further investigations. IAG University of Stuttgart provided an airfoil data set synthesized from 3D rotational CFD

305 computations employing the azimuthal averaging method as described in (Hansen et al., 1997) and (Bangga, 2018). Two participants then re-simulated Case IV.2.1 with their BEM codes. The resulting normal force trends are given in Figure 11.

(a) Fn, r/R=33%

(b) Fn, r/R=48%
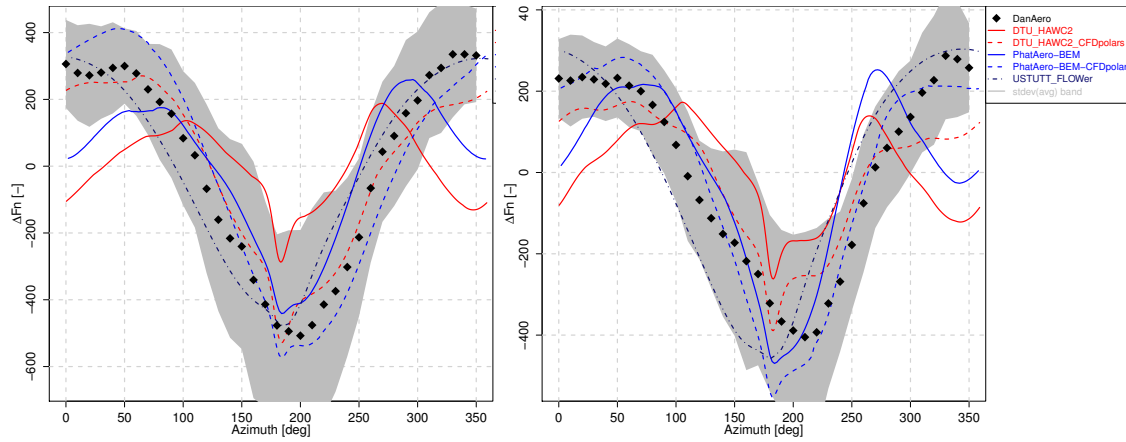
(c) Fn, r/R=76%

(d) Fn, r/R=92%
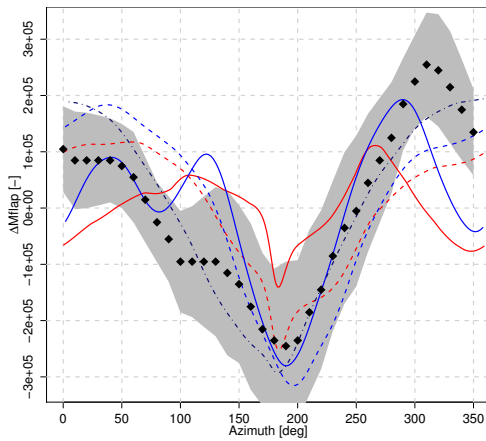
(e) Mflap
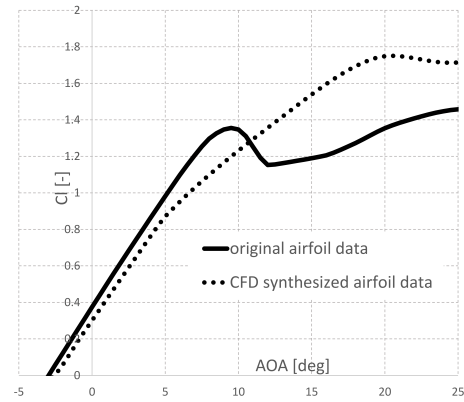
(f) Lift curves at r/R=48%

Figure 11. Normal force Fn variation and airfoil data using CFD synthesized airfoil data, Case IV.2.1. USTUTT reference CFD data is plotted as well.

It is clear that for Case IV.2.1 the results featuring the CFD synthesized polars (dashed lines) outperform the results with the original polars. This indicates the earlier found discrepancies to be airfoil data related. It is noted that the airfoils are operating in the stall region and apparently the stall delay due to the 3D rotational and unsteady effects is not correctly taken into account by the original airfoil data (despite the fact that a 3D-correction was applied (Bak and Fuglsang, 2004)). Additionally it was found that application of a classical 3D-correction model like Snel Snel et al. (1993) also can not predict the stall delay correctly. Comparing the underlying polars at r = 48%R in Figure 11f clearly shows the stall delay as predicted by CFD. This explains, in the case of a downward pointing blade when using the original airfoil data, the loading and induction augmentation as the lift increases for a decreasing angle of attack (when coming back from stall around 12°). It is noted that, although this reversed trend is most apparent for the 48%R station, the CFD synthesized airfoil data clearly improves the agreement with measurements also for the outboard stations. This observation hints at the need for a stall delay model that works along the whole blade span instead of only the inboard part. For Case IV.2.2, which is dominated by induction aerodynamics and featuring angles of attack further away from stall, it can be shown that the CFD synthesized polars hardly impact the trend variation.

5 Conclusions

A large comparison exercise has been performed featuring three simulation cases in axial, sheared and yawed inflow conditions. Results were obtained from more than 19 simulation tools originating from 12 institutes ranging in fidelity from BEM to CFD and compared to state-of-the-art field measurements from the DanAero turbine. More than 15 different variable types ranging from lifting line variables to pressures, loads and velocities have been compared for the different conditions, resulting in over 250 comparison plots. The result is a unique insight in the current status and accuracy of rotor aerodynamic modeling.

For axial flow conditions, a good agreement was found between the various code types, where a dedicated grid sensitivity study was necessary for the CFD simulations. However, compared to wind tunnel experiments that feature controlled conditions (like New Mexico), it remains a challenge to achieve good agreement of absolute levels between simulations and measurements in the field. Considerable efforts were spent on investigating possible causes in the measurements for the deviations to the simulations without success. For sheared inflow conditions, uncertainties due to rotational effects on airfoil data result in the CFD results to stand out above the codes that need input of sectional airfoil data. However, it was demonstrated that using CFD synthesized airfoil data is an effective means to bypass this shortcoming. For yawed flow conditions, it was observed that modeling of the skewed wake effect is still problematic for BEM codes, whereas CFD and FVW codes inherently model the underlying physics correctly. The next step is a comparison in turbulent inflow conditions, which is featured in IEA Wind Task 47.

Doing this analysis in cooperation under the auspices of IEA TCP Wind has led to many mutual benefits for the participants. The large size of the consortium brought ample manpower for the analysis where the learning process by combining several complementary experiences and modeling techniques gave valuable insights that could not be found when the analysis was carried out individually.

References

355 IEA TCP Wind website, https://iea-wind.org/, 2021.

Bak, C. and Fuglsang, P.: A Method for Deriving 3D Airfoil Characteristics for a Wind Turbine, in: 42th AIAA Aerospacce Sciences Meeting and Exhibit, AIAA-2004-0666, Reno, Nevada, 2004.

Bak, C., Madsen, H., Paulsen, U. S., Gaunaa, M., Sørensen, N., Fuglsang, P., Romblad, J., Olsen, N., Enevoldsen, P., Laursen, J., and Jensen, L.: DAN-AERO MW: Detailed aerodynamic measurements on a full scale MW wind turbine, European Wind Energy Conference and
360 Exhibition 2010, Ewec 2010, 2, 792–836, 2010.

Bak, C., Madsen, H., Troldborg, N., Gaunaa, M., Skrzypinski, W., Fischer, A., Paulsen, U., Møller, R., Hansen, P., Rasmussen, M., , and Fuglsang, P.: DANAERO MW: Instrumentation of the NM80 turbine and meteorology mast at Tjæreborg, Report-I-0083, DTU Wind Energy, 2013.

Bangga, G.: Comparison of Blade Element Method and CFD Simulations of a 10 MW Wind Turbine, Fluids, 3, 73, 2018.

365 Bauchau, O., Bottasso, C., and Nikishkov, Y.: Modeling rotorcraft dynamics with finite element multibody procedures, Mathematical and Computer Modelling, 33, 1113 – 1137, https://doi.org/10.1016/S0895-7177(00)00303-4, 2001.

Blondel, F., Galinos, C., Paulsen, U., Bozonnet, P., Cathelain, M., Ferrer, G., Madsen, H., Pirrung, G., and Silvert, F.: Comparison of Aero-Elastic Simulations and Measurements Performed on NENUPHAR's 600kW Vertical Axis Wind Turbine: Impact of the Aerodynamic Modelling Methods, Journal of Physics: Conference Series, 1037, 022 010, https://doi.org/10.1088/1742-6596/1037/2/022010, 2018.

370 Boorsma, K.: Wind Tunnel Rotor Measurements, in: Handbook of Wind Energy Aerodynamics, Springer, Cham, https://doi.org/10.1007/978-3-030-05455-7_30-1, 2021.

Boorsma, K., Grasso, F., and Holierhoek, J.: Enhanced approach for simulation of rotor aerodynamic loads, Tech. Rep. ECN-M–12-003, ECN, presented at EWEA Offshore 2011, Amsterdam, 29 November 2011 - 1 December 2011, 2011.

Boorsma, K., Schepers, J., Gomez-Iradi, S., Herraez, I., Lutz, T., Weihing, P., Oggiano, L., Pirrung, G., Madsen, H., Shen, W., Rahimi, H.,
375 and Schaffarczyk, P.: Final report of IEA Task 29, Mexnext (Phase 3): Analysis of MEXICO wind tunnel measurements, ECN-E-18-003, Energy Research Center of the Netherlands, 2018.

Bozonnet, P., Caille, F., Blondel, F., Melis, C., Poirette, Y., and Perdrizet, T.: A Focus on Fixed Wind Turbine Tests to Improve Coupled Simulations of Floating Wind Turbine Model Tests, 2017.

Cambier L., V. J.-P.: Status of the elsA CFD software for Flow Simulation and Multidisciplinary Applications, in: Proceedings of 46th AIAA
380 Aerospace Science Meeting and Exhibit, 2008.

Collier, W.: A Consistent Structural Damping Model for Integrated and Superelement Modelling of Offshore Wind Turbine Support Structures in Wind Turbine Design Software Bladed, International Conference on Offshore Mechanics and Arctic Engineering, 59353, 2019.

Fefferman, C. L.: Existence and smoothness of the Navier-Stokes equation, The millennium prize problems, 57, 67, 2000.

Greco, L. and Testa, C.: Wind turbine unsteady aerodynamics and performance by a free-wake panel method, Renewable Energy, 164,
385 444–459, 2021.

Hand, M., Simms, D., Fingersh, L., Jager, D., Cotrell, J., Schreck, S., and Larwood, S.: Unsteady Aerodynamics Experiment Phase VI Wind Tunnel Test Configurations and Available Data Campaigns, NREL/TP-500-29955, National Renewable Energy Laboratory, NREL, 2001.

Hansen, M., Sørensen, N., et al.: AVATAR Deliverable D2.4: Aerodynamics of Large Rotors, 2016.

Hansen, M. O., Sørensen, N. N., and Michelsen, J.: Extraction of lift, drag and angle of attack from computed 3-D viscous flow around a
390 rotating blade, in: 1997 European Wind Energy Conference, 1997.

Kroll, N., Rossow, C.-C., Becker, K., and Thiele, F.: The MEGAFLOW project, Aerospace Science and Technology, 4, 223–237, 2000.

Le Cunff, C., Heurtier, J., Piriou, L., Berhault, C., Perdrizet, T., Teixeira, D., Ferrer, G., and Gilloteaux, J.: Fully Coupled Floating Wind Turbine Simulator Based on Nonlinear Finite Element Method: Part I - Methodology, Volume 8: Ocean Renewable Energy, https://doi.org/10.1115/OMAE2013-10780, v008T09A050, 2013.

395 Madsen, H., Bak, C., Dossing, M., Mikkelsen, R., and Oye, S.: Validation and modification of the Blade Element Momentum theory based on comparisons with actuator disc simulations, Wind Energy, 13, 373–389, https://doi.org/10.1002/we.359, 2010a.

Madsen, H., Bak, C., Paulsen, U., Gaunaa, M., Sørensen, N., Fuglsang, P., Romblad, J., Olsen, N., Enevoldsen, P., Laursen, J., and Jensen, L.: The DAN-AERO MW Experiments, 48th Aiaa Aerospace Sciences Meeting Including the New Horizons Forum and Aerospace Exposition, pp. 2010–0645, 2010b.

400 Madsen, H., Larsen, T. J., Pirrung, G., Li, A., and Zahle, F.: Implementation of the Blade Element Momentum Model on a Polar Grid and its Aeroelastic Load Impact, Wind Energy Science, 5, 1–27, https://doi.org/10.5194/wes-2019-53, 2020.

Meyer Forsting, A., Pirrung, G., and Ramos-Garcia, N.: A vortex-based tip/smearing correction for the actuator line, Wind Energy Science, 4, 369–383, 2019.

Michelsen, J.: Basis3D - A Platform for Development of Multiblock PDE Solvers., Tech. rep., Risø National Laboratory, 1992.

405 Moriarty, P. J. and Hansen, A. C.: AeroDyn Theory Manual, Tech. rep., National Renewable Energy Laboratory, nREL/EL-500-36881, 2005.

Mudry, M.: La théorie des nappes tourbillonnaires et ses applications à l'aérodynamique instationnaire, PhD Thesis, Paris VI University, 1982.

Perdrizet, T., Gilloteaux, J., Teixeira, D., Ferrer, G., Piriou, L., Cadiou, D., Heurtier, J., and Le Cunff, C.: Fully Coupled Floating Wind Turbine Simulator Based on Nonlinear Finite Element Method: Part II - Validation Results, Volume 8: Ocean Renewable Energy,
410 https://doi.org/10.1115/OMAE2013-10785, v008T09A052, 2013.

Pirrung, G., Riziotis, V., Aagaard Madsen, H., Hansen, M., and Kim, T.: Comparison of a Coupled Near and Far Wake Model With a Free Wake Vortex Code, Wind Energy Science, 2, 15–33, https://doi.org/10.5194/wes-2016-2, 2017.

Pirrung, G. R., Aagaard Madsen, H., Kim, T., and Heinz, J. C.: A coupled near and far wake model for wind turbine aerodynamics, Wind Energy, 19, 2053–2069, https://doi.org/10.1002/we.1969, 2016.

415 Schepers, J.: Engineering models in wind energy aerodynamics, development, implementation and analysis using dedicated aerodynamic measurements, Ph.D. thesis, University of Delft, ISBN 978-94-6191-507-8, 2012.

Schepers, J., Brand, A., Bruining, A., Graham, J., Hand, M., Infield, D., Madsen, H., Paynter, J., and Simms, D.: Final Report of IEA Annex XIV: Field Rotor Aerodynamics, Tech. rep., ECN-C–97-027, 1997.

Schepers, J., Boorsma, K., T.Cho, Gomez-Iradi, S., Schaffarczyk, P., Jeromin, A., Shen, W., Lutz, T., Meister, K., Stoevesandt, B., Schreck,
420 S., Micallef, D., Pereira, R., Sant, T., Madsen, H., and Sorensen, N.: Final report of IEA Task 29, Mexnext (Phase 1): Analysis of MEXICO wind tunnel measurements, ECN-E-12-004, Energy Research Center of the Netherlands, 2012.

Schepers, J., Boorsma, K., Gomez-Iradi, S., Schaffarczyk, P., Madsen, H., Sorensen, N., Shen, W., Lutz, T., Schulz, C., Herraez, I., and Schreck, S.: Final report of IEA Task 29, Mexnext (Phase 2), ECN-E-14-060, Energy Research Center of the Netherlands, 2014.

Schepers, J., Boorsma, K., Madsen, H., Pirrung, G., Ozcakmak, O., Bangga, G., Guma, G., Lutz, T., Potentier, T., Braud, C., Guilmineau,
425 E., Croce, A., Cacciola, S., Schaffarczyk, A., Lobo, B., Ivanell, S., Asmuth, H., Bertagnolio, F., Sorensen, N., Shen, W., Grinderslev, C., Forsting, A., Blondel, F., Bozonnet, P., Boisard, R., Yassin, K., Honing, L., Stoevesandt, B., Imiela, M., Greco, L., Testa, C., Magionesi, F., Vijayakumar, G., Ananthan, S., Sprague, M., Branlard, E., Jonkman, J., Carrion, M., Parkinson, S., and Cicirello, E.: IEA Wind TCP Task 29, (Phase IV): Detailed Aerodynamics of Wind Turbines, Tech. rep., https://doi.org/10.5281/zenodo.4813068, 2021.

Schepers, J. et al.: Final report of IEA Annex XVIII' Enhanced Field Rotor Aerodynamics Database, ECN-C-02-016, Energy Research
    Centre of the Netherlands, ECN, 2002.

430

Schreck, S.: IEA Wind Annex XX: HAWT Aerodynamics and Models from Wind Tunnel Measurements, NREL/TP-500-43508, The Na-
    tional Renewable Energy Laboratory, NREL, 2008.

Schwamborn, D., Gerhold, T., and Heinrich, R.: The DLR TAU-Code: Recent Applications in Research and Industry., in: European Confer-
    ence on Computational Fluid Dynamics, 2006.

435 Shaler, K., Branlard, E., and Platt, A.: OLAF User's Guide and Theory Manual, Tech. rep., National Renewable Energy Laboratory, 2020.

Simms, D., Schreck, S., Hand, M., and Fingersh, L.: NREL Unsteady Aerodynamics Experiment in the NASA-Ames Wind Tunnel: A
    Comparison of Predictions to Measurements, NREL/TP-500-29494, The National Renewable Energy Laboratory, NREL, 2001.

Snel, H., Houwink, R., van Bussel, G., and Bruining, A.: Sectional prediction of 3D effects for stalled flow on rotating blades and comparison
    with measurements, in: Proc. European Community Wind Energy Conference, 1993.

440 Sprague, M., Ananthan, S., Vijayakumar, G., and Robinson, M.: ExaWind: A multi-fidelity modeling and simulation environment for wind
    energy, in: Proceedings of NAWEA WindTech, 2019.

Sørensen, J. N. and Shen, W. Z.: Numerical modeling of wind turbine wakes, Journal of Fluids Engineering, 124, 393–399, 2002.

van Garrel, A.: Development of a wind turbine aerodynamics simulation module, Tech. Rep. ECN-C–03-079, ECN, 2003.